

1 Wet-Radome Attenuation in ARM Cloud Radars and Its Utilization in Radar Calibration Using Disdrometer
2 Measurements

3
4 Min Deng¹, Scott E. Giangrande¹, Michael P. Jensen¹, Karen Johnson¹, Christopher R. Williams²,
5 Jennifer M. Comstock³, Ya-Chien Feng³, Alyssa Matthews³, Iosif A. Lindenmaier³, Timothy G.
6 Wendler³, Marquette Rocque³, Aifang Zhou¹, Zeen Zhu¹, Edward Luke¹, and Die Wang¹

7
8
9 ¹ Brookhaven National Laboratory, Environmental and Climate Sciences Department, Upton,
10 New York

11 ² University of Colorado Boulder, Colorado Center for Astrodynamics Research, Boulder,
12 Colorado

13 ³ Pacific Northwest National Laboratory, Richland, Washington

14
15
16 *Correspondence to:* Min Deng (mdeng@bnl.gov)

17
18
19 Manuscript to be submitted to AMT publication.

20
21
22
23
24
25
26
27
28
29
30
31
32
33
34

35 Abstract

36

37 A relative calibration technique has been developed for the U.S. Department of Energy's
38 (DOE) Atmospheric Radiation Measurement (ARM) user facility Ka-Band ARM Zenith Radars
39 (KAZRs). This method uses the signal attenuation caused by water on the radome to estimate
40 reflectivity factor (Z_e) offsets. The wet-radome attenuation (WRA) is assumed to follow a log-
41 linear relationship with rainfall rate during light and moderate rain, as measured by a collocated
42 surface disdrometer. The technique has an uncertainty of approximately 3 dB, due to factors such
43 as disdrometer measurement error, rain variability between radar and disdrometer sample volumes,
44 and the fitting function's uncertainty for the WRA behavior. A practical advantage of this WRA-
45 based approach to shorter-wavelength radar monitoring is that, while it requires a reference
46 disdrometer, it proves feasible for a wider range of collocated disdrometer measurements
47 compared to traditional direct disdrometer comparison at the onset of light rain. This technique
48 thus offers a cost-effective monitoring tool for remote or long-term radar deployments.

49 This calibration technique was applied during the ARM TRacking Aerosol Convection
50 interactions ExpeRiment (TRACER) from October 2021 through September 2022. The estimated
51 Z_e offsets were compared against traditional radar calibration and monitoring methods using
52 available datasets from this campaign. Results show that the WRA-based offsets align closely with
53 mean offsets found between cloud radars and from direct disdrometer comparison near the onset
54 of rain, while also reflecting similar offset and campaign-long trends when compared to collocated,
55 independently calibrated radar wind profiler. Nevertheless, overall, the KAZR Z_e offsets estimated
56 during TRACER remained stable at approximately 2 dB lower than the disdrometer estimates from
57 the campaign start until the end of June 2022, afterward, the offsets increased to around 7 dB by
58 the campaign's end. This increase is linked to a drop of about 1 dB in transmitter power toward
59 the end of the project.

60

61

62

63

Deleted: Z

Deleted: Z

66

67 Short Summary

68

69 A relative calibration technique is developed for the cloud radar by monitoring the intercept of the
70 wet-radome attenuation log-linear behavior as a function of rainfall rates in light and moderate
71 rain conditions. This resulted KAZR Ze offset during the ARM TRACER campaign is compared
72 favorably with the traditional disdrometer comparison near the rain onset, while also demonstrates
73 similar trends with respect to collocated and independently calibrated reference radars.

74

75

76

77 1 Introduction

78 The U.S. Department of Energy (DOE) Atmospheric Radiation Measurement (ARM) user
79 facility operates millimeter-wavelength cloud radars (35 and 94 GHz) at various global fixed and
80 mobile sites (e.g., Mather and Voyles, 2013; Miller et al., 2016; Kollias et al., 2007, 2020). These
81 "cloud" radars are often more sensitive than traditional centimeter-wavelength weather radars,
82 allowing them to detect cloud droplets more effectively. However, this sensitivity comes with a
83 trade-off, as shorter wavelengths are prone to partial or complete attenuation in clouds and
84 precipitation. Such attenuation introduces uncertainties in key radar-derived properties like
85 reflectivity factor (Z_e), affecting cloud and hydrological retrieval accuracy (e.g., Matrosov, 2005;
86 Deng et al., 2014; Zhu et al., 2019).

87 Given the importance of accurate Z_e measurements, the routine deployment and operation
88 of cloud radars necessitate frequent calibration and monitoring activities. In general, more rigorous
89 radar calibration efforts can be implemented (e.g., Russchenberg et al., 2020), but these approaches
90 are often system-specific and require highly skilled engineers or technicians, significant time, and
91 specialized equipment (within ARM, e.g., Mead, 2010). For weather and climate applications,
92 radar-based research has increasingly turned to "relative" calibration techniques, which rely on Z_e
93 estimates from nearby reference instruments or expectations based on intrinsic properties of the
94 hydrometeors or other media (e.g., Bringi and Chandrasekar, 2001; Giangrande et al., 2005; Protat
95 et al., 2011; Kollias et al., 2019; Maahn et al., 2019; Williams et al., 2023). Several of these
96 "natural" calibration concepts have proven effective for quantifying radar performance in many

97 hydrological applications requiring Z_e estimates within 2-3 dB. The simplest approach is often a
98 cross-comparison of Z_e characteristics with collocated, calibrated reference radars. For example,
99 extended comparisons of clouds near ARM ground sites using CloudSat radar measurements have
100 successfully monitored the long-term ARM cloud radar record (Protat et al., 2011; Kollias et al.,
101 2019). For finer-scale comparisons during ARM deployments, the Ka-Band ARM Zenith Radar
102 (KAZR) is often collocated with a Radar Wind Profiler (RWP, 915 or 1290 MHz) and the Ka- and
103 X-band Scanning ARM Cloud Radar (KaSACR/ XSACR), which are easier to monitor using
104 independent techniques better suited to scanning and/or longer-wavelength radar.

Deleted: Z

105 Among the various methods of relative cloud radar monitoring, a common approach relies
106 on surface disdrometer observations. The reflectivity factor can be estimated for assumed rain
107 properties using techniques such as T-matrix scattering algorithms applied to the drop size
108 distribution of rain measured by the surface disdrometer (Mishchenko et al., 1996). Comparing
109 radar-measured reflectivity near the surface with disdrometer-estimated reflectivity provides a
110 common way to estimate radar calibration offsets (e.g., Kollias et al., 2019; Myagkov et al., 2020;
111 Russchenberg et al., 2020; and Lamer et al., 2021). Disdrometer comparison techniques like this
112 have been implemented as routine procedures for radar monitoring, such as in the Aerosol Cloud
113 Tracer Gas Research Infrastructure (ACTRIS) network in Europe (Dupont et al., 2022). For radars
114 that experience negligible attenuation in rain, such procedures are often straightforward to
115 implement across a variety of widespread precipitating conditions (e.g., Williams et al., 2023).
116 However, for shorter radar wavelengths, where gaseous attenuation, rain attenuation, and wet-
117 radome attenuation are not negligible, applying this approach can be more complicated.

118 Specifically, the two-way attenuation associated with radome wetting (referred to here as
119 wet radome attenuation or WRA) is a well-known phenomenon. During rainfall, water droplets
120 bead on the surface of the radar radome, forming a wet film that eventually flows off the radome
121 once it reaches sufficient mass, similar to the water layer on a car window. Droplets impacting the
122 radome during persistent rain further alter the water depth through bouncing and splashing (Gibble,
123 1964; Anderson, 1975; Yu et al., 2021). For long-wavelength radars, WRA is often considered
124 negligible (Thompson et al., 2012; Kurri and Huuskonen, 2008). However, for shorter-wavelength
125 radars, the impact of WRA is potentially more significant. For example, at X-band, Bechini et al.
126 (2010) and Gorgucci et al. (2013) observed a loss of 5 dB in moderate rain by comparing
127 simultaneous X-band radar measurements using spherical radomes with a collocated video

Deleted: at close range

130 disdrometer. This WRA has been shown to depend on the thickness of the water film (d) on the
131 radome, which in turn is a function of rain rate, as described by the Gibble formula (Gibble, 1964;
132 Anderson, 1975):

$$133 \quad d = \left(\frac{3\mu_k r R}{2g} \right)^{1/3}, \quad (1)$$

134 where μ_k is the kinematic viscosity of water (that also varies with temperature), r is the radome
135 radius, R is the rain rate, and g is the gravitational acceleration. Additional relations between WRA
136 and R have been developed based on the Gibble's $R^{1/3}$ formula by Frasier et al. (2013) and
137 Gorgucci et al. (2013) for X-band radar calibration studies.

138 Few studies have considered WRA for assessing cloud radar offsets at Ka-band (35 GHz).
139 As the water absorption coefficient is inversely proportional to wavelength (Bertie et al. 1996,
140 Segelstein 1981), the WRA at Ka-band is approximately as three times as that at X-band for the
141 same depth of rainwater on the radome. It is understood that WRA will impact direct estimates of
142 the offset between cloud radar and disdrometer Z_e estimates in rainy conditions, and faulty offset
143 assessment after rain ends may occur owing to extended radome drying delays. Therefore, direct
144 comparison concepts previously cited typically consider only the periphery cloud, drizzle or light
145 rain conditions (i.e., $R < 1\text{-}2 \text{ mm hr}^{-1}$) at the onset of a rainfall event to minimize various forms of
146 attenuation. This often is a very stringent and subjective employment of these conditions: First, it
147 limits the opportunities for direct disdrometer monitoring of cloud radar to a selected window of
148 rainfall rates and event timing. Identifying these light rain or drizzling conditions is also contingent
149 on the requirements for collecting high-quality disdrometer measurements (i.e., those that require
150 significant droplet number counts), wherein a separate rain rate cut-off may be required to avoid
151 significant WRA. Overall, it is potentially useful to establish other forms of cloud radar monitoring
152 that could benefit from a wider range of observations collected during precipitation window.

153 In this study, we first identify intervals of WRA for Ka-band radars by comparing
154 observations from ARM's KAZR with a collocated suite of instruments, including a surface
155 disdrometer, a calibrated RWP, and KaSACR/XSACR observations collected in vertical pointing
156 (VPT) modes during the Tracking Aerosol Convection Interactions Experiment (TRACER). We
157 then develop a new WRA fitting technique and apply it to calibrate the Z_e offset for KAZR using
158 TRACER measurements. The performance of this technique is evaluated against three traditional

159 relative calibration or monitoring methods for Ka-band radar: (i) direct disdrometer comparisons
160 of Ze in light rain at the onset of rain events, (ii) a cross-comparison with independently calibrated
161 RWP measurements, and (iii) a cross-comparison with collocated scanning KaSACR
162 measurements.

163 The paper is organized as follows. Section 2 introduces the radar datasets and supporting
164 TRACER datasets used in this study. In Section 3, a relative calibration technique is developed
165 with daily KAZR and KaSACR measurements collected during light and moderate rainfall
166 conditions. In Section 4, the technique is applied to the KAZR measurements during the TRACER
167 campaign to assess the long-term calibration offset trend for KAZR, and the result is evaluated
168 against other calibration methods. A summary of the performance of this WRA technique for
169 relative offset monitoring is provided in Section 5.

170

171 2 TRACER Dataset Description and Comparisons

172 The TRACER campaign took place in the Houston, TX region from 1 October 2021 to 30
173 September 2022 (Jensen et al., 2019, 2022, and 2023) with a goal of studying the interactions of
174 aerosols and convective clouds. The main surface measurement site was located at La Porte, TX
175 housed the deployment of the first ARM Mobile Facility (AMF1; Miller et al., 2016). The AMF1
176 consists of several ground-based remote-sensing and profiling instruments, and included the
177 deployment of the KAZR, KaSACR/XSACR, and radar wind profiler (RWP) units that serve as
178 the radars for this study. The surface instrumentation also included multiple laser and video
179 disdrometers as reference anchors.

180

181 2.1 TRACER Cloud Radars (KAZR and KaSACR/XSACR)

182 The KAZR (Widener et al., 2012) is a successor to ARM’s highly successful millimeter-
183 wavelength cloud radar (MMCR). The KAZR has a flat radome inclined at 4°. A complete list of
184 KAZR specifications is provided in Table 1. The KAZR transmits and receives two types of pulses:
185 (i) the burst pulse, a simple narrow pulse of radio-frequency energy (referred to as “GE” mode),
186 and (ii) the chirp pulse, a longer, frequency-modulated pulse with higher transmitted energy and
187 greater sensitivity, but with data collection starting at a higher range due to the larger blind zone
188 imposed by the longer pulse length (referred to as “MD” mode). Although the MD mode is more

189 sensitive to clouds (i.e., has a lower minimum detectable Z_e), only the KAZR GE mode data are
190 used for disdrometer comparisons, as near-surface observations are required.

191 The KaSACR and XSACR are co-mounted on a scanning pedestal (Kollias et al., 2014a,
192 2014b). During TRACER, the KaSACR/XSACR typically followed a 10-minute scanning pattern:
193 (i) two low-level plan position indicator (PPI) scans at 1° and 2° elevation, followed by (ii) 6
194 hemispheric range height indicator (HSRHI) scans at 30° azimuth intervals, and then (iii) 2 minutes
195 of vertical pointing (VPT) mode. This study utilizes the 2-minute VPT mode segment from each
196 10-minute scanning sequence (i.e., nominal scanning VPT mode). The specifications during VPT
197 mode are listed in Table 1. For one event on September 3-4, 2022, the KaSACR/XSACR was
198 temporarily operated exclusively in VPT mode (i.e., stationary VPT mode) for radar cross-
199 calibration purposes. The KaSACR has an inclined radome similar to the KAZR but is relatively
200 newer, with potentially less deterioration of its hydrophobic coating. The XSACR has a conical
201 radome with a slant angle of 45° to the surface. Overall, the WRA effect is expected to be smaller
202 for the XSACR compared to either Ka-band radar, due to wavelength-dependent differences as
203 well as the improved radome design. The KaSACR calibration offsets between May and
204 September 2022 are expected to be stable based on ground clutter analysis using relative
205 calibration adjustment (RCA) techniques (Skolnik, 2000; Hunzinger et al., 2020) and are reported
206 to be close to 0 dB, according to the ARM TRACER radar b1 data processing report (Feng et al.,
207 2024).

208 To compare with Z_e estimates from disdrometer measurement, radar measurements at 500
209 m are selected and corrected for gaseous attenuation using nearby radiosonde measurements (e.g.,
210 Ulaby et al., 1981). Rain attenuation is also corrected using specific attenuation coefficient (K)
211 estimates from disdrometer measurement, assuming a uniform layer between the surface and 500
212 m. There is concern that the radar might saturate, particularly for the KaSACR near its minimum
213 range, which could introduce a low bias in measured Z_e compared to disdrometer Z_e . Based on
214 communication with an ARM radar engineer, the power associated with the highest voltage
215 digitizable by the radar's Analog-to-Digital Converter (ADC) is 5.9 dBm. The corresponding
216 KAZR saturation reflectivity at 500 meters is approximately 45 dBZ, given its calibration constant
217 of -12 dBm. Similarly, the KaSACR saturation reflectivity at 500 m is about 31 dBZ, given its
218 calibration constant of -26 dBm. The measured radar reflectivities from both KAZR and KaSACR

219 at 500 m are generally less than 25 dBZ, well below the saturation threshold. Additional supporting
220 evidence through radar profile comparisons can be found in the supplementary material.

221

222 2.2 Surface Disdrometer Measurements and Value-Added Products

223 A Parsivel2 laser disdrometer (LDIS) and a two-dimensional video disdrometer (VDIS)
224 unit were deployed at the main site during TRACER in very close proximity to the cloud radars.
225 For disdrometer geophysical quantities and data quality control, procedures follow the standard
226 drop size distribution (DSD) filtering in Giangrande et al. (2019) implemented by ARM in their
227 precipitation value-added products (Video Disdrometer Quantities--VDISQUANTS and Laser
228 Disdrometer Quantities--LDQUANTS, Hardin et al., 2020). These products employ several fall
229 speed checks, temperature, drop shape/canting assumptions, larger drop restrictions (no drop sizes
230 > 5 mm) and drop count thresholds (> 20 drops per minute for a valid DSD) that impact estimates
231 of hydrometeor Z_e and K for radar frequencies using a T-matrix scattering algorithm (Mishchenko
232 et al., 1996). As further discussed within the disdrometer literature (Tokay et al., 2001, 2013;
233 Giangrande et al., 2019; Wang et al., 2021), the VDIS is considered the more reliable and sensitive
234 disdrometer to a wider range of drop sizes under nominal light rain operating conditions.
235 Therefore, the estimated Z_e at Ka-band in VDISQUANTS is used within this study as our ground
236 truth for KAZR calibration and surface rain rate, while the LDIS products have been used as an
237 independent reference for monitoring RWP Z_e estimates (e.g., Williams et al., 2023), which is
238 required for additional direct radar comparisons in Section 4.

239

240 2.3 Radar Wind Profiler (RWP)

241 The RWP deployed during TRACER was operated using an adaptive scanning mode,
242 switching between a traditional boundary layer horizontal wind mode and a vertically pointing
243 precipitation mode adopted by ARM for its recent deep convective cloud campaigns (e.g., Tridon
244 et al., 2013; Giangrande et al., 2013, 2016). When the signal-to-noise ratio in the vertical beam
245 exceeded a predefined threshold, the RWP switched into this precipitation mode and employs a
246 single vertically pointing beam operation. This mode transmitted short- and long-pulses to observe
247 echoes close to the radar with fine resolution, or further from the radar with coarser
248 resolution. Important to this study, the TRACER RWP mode switching sometimes prevented the
249 RWP from immediately observing the periphery lightly precipitating clouds as they passed over

250 the AMF1 site. However, this mode-switching sampling issue does not impact the bulk KAZR-
251 RWP Ze cross-comparisons because we primarily consider daily average behaviors. As before, the
252 RWP Ze measurements in precipitation mode were calibrated independently using collocated
253 LDIS observations (i.e., Williams et al., 2023), who found a standard deviation of 2 - 4 dB between
254 the RWP at 500 m and LDIS.

Deleted: Z

255
256 3 Cloud Radar Ze Calibration and Monitoring: Development of a New WRA Technique

257

258 3.1 Identification of WRA: KaSACR/XSACR in Stationary VPT Modes

259

260 Figure 1a-c show the measured reflectivity (Z_e) from the KaSACR/XSACR and the KAZR
261 GE mode on 03-04 September 2022, when the KaSACR/XSACR was operated exclusively in a
262 stationary vertically pointing (VPT) mode. Two intervals of widespread rainfall were captured: the
263 first around 17-19 UTC and the second from 20–02 UTC. A radar "bright band" signature,
264 indicative of the melting level, appears around 5 km AGL during this event. After 02 UTC (20
265 LT), light rain gave way to high, scattered clouds through the night, until thick anvil clouds from
266 nearby convection moved in around 15 UTC (09 LT). Overall, the KaSACR/XSACR reported
267 similar Z_e values under peripheral cloudy conditions and during light rain, where rain attenuation
268 and WRA were minimal. As expected, larger discrepancies between XSACR and KaSACR (with
269 the KaSACR showing lower, attenuated Z_e values) occurred during heavier rainfall from 22-00
270 UTC. The KAZR consistently reported lower Z_e values than the KaSACR, with differences often
271 exceeding 5 dB throughout the event.

Deleted: Z

272 The Z_e difference between the KaSACR and KAZR values in Fig.1d exhibits strong
273 temporal variation but limited vertical variation, indicating that the difference is likely driven by
274 the radar or its local environment (e.g., WRA) rather than atmospheric features. The minimum
275 difference of ~7 dB in high clouds, observed around 17-18 UTC and again the next morning (15-
276 17 UTC on 4 September), suggests an overall Z_e offset between the KAZR and KaSACR. A
277 minimum difference of ~7 dB in rain (at 19, 21, and 23 UTC) indicates similar WRA behavior for
278 both KAZR and KaSACR. However, a prolonged increase in this difference after moderate rain,
279 especially under humid conditions at night (0-12 UTC, or 18-6 LT), suggests that the KAZR and
280 KaSACR may experience additional discrepancies after rain or in high humidity, possibly due to
281 the older, less hydrophobic radome of the KAZR, as noted in the Cloud, Aerosol, and Complex

284 Terrain Interactions (CACTI) campaign (Varble et al. 2021; Hardin et al. 2020). Accurate
285 correction for KAZR wet-radome attenuation is challenging and beyond the scope of this study;
286 however, WRA behavior in rain can provide a basis for tracking KAZR calibration, as will be
287 demonstrated in the following sections.

288 The time series of rain rate (R), K and Z_e estimates at Ka- and X-bands from
289 VDISQUANTS for the 03-04 September 2022 case are shown in Fig. 2a and b. The sampled R
290 from the disdrometer is commonly less than 1 mm hr^{-1} , but approach 5 mm hr^{-1} around 2330 UTC.
291 The Z_e from KAZR, KaSACR/ XSACR at 500 m are plotted in Fig. 2b. For all collocated
292 precipitating samples, the XSACR Z_e (black crosses) has a high correlation with estimated Z_e (r_r
293 = 0.95), while KAZR Z_e (blue crosses) are biased low when directly compared to the disdrometer
294 Z_e , which is exacerbated further in heavy rain contexts. KaSACR Z_e (red cross) falls in between
295 XSACR and KAZR Z_e values.

296 Figure 2c shows the differences between measured and estimated Z_e (Dze) for KAZR,
297 KaSACR, and XSACR. The XSACR exhibits a minimum Dze of 0 dB when the rain rate is below
298 0.1 mm hr^{-1} , but this difference can reach 5 dB around 23:30 UTC. The KaSACR Dze is
299 approximately 1 dB at 18 and 21 UTC, while the KAZR Dze is around 7 dB, suggesting calibration
300 offsets of around 1 dB for KaSACR and 7 dB for KAZR. Both KaSACR and KAZR Z_e are further
301 biased lower by an additional 13 dB when the rain rate reaches approximately 5 mm hr^{-1} around
302 23:30 UTC. This 13 dB reduction in KAZR and KaSACR estimates is significantly larger than the
303 expected two-way attenuation in rain at Ka-band ($\sim 2 \text{ dB}$, Figure 2a), suggesting that other factors,
304 such as WRA, contribute increasingly to the observed offset in rain. Additionally, WRA for both
305 KAZR and KaSACR likely shows similar dependence on rain rates.

306 The estimated Z_e from VDISQUANTS during the entire TRACER campaign are plotted as a
307 function of R in Fig. 3. The estimated Z_e for both X- and Ka-bands exhibits a log-linear
308 relationship with R . When R exceeds 2 mm hr^{-1} , the Z_e values begin to diverge, and the difference
309 between the two wavelengths increases as R rises, likely due to resonance effects associated with
310 non-Rayleigh scattering (Baldini et al., 2012). The Z-R relation is fitted in black line with $Z =$
311 $200R^{1.4}$, which is slightly smaller than the WSR-88D Z-R relation in convective summer deep
312 convection ($Z = 300R^{1.4}$, Crosson, 1996). The cumulative probability distribution (CDF) of rain
313 rates (red line in Figure 3) shows that about 15% of disdrometer samples have $R < 0.1 \text{ mm hr}^{-1}$,

Deleted: Z

Formatted: Indent: First line: 0"

315 indicating limited data for traditional direct disdrometer comparison at precipitation onset.
316 However, approximately 85% of TRACER data samples have $R < 5 \text{ mm hr}^{-1}$, suggesting that this
317 large range of data sample is suitable for the WRA technique applications discussed in the
318 following sections.

319 3.2 Identification of WRA: KaSACR/XSACR in its Scanning-VPT Mode

320
321 To further illustrate the WRA, we compared radar and disdrometer measurements while
322 the KaSACR/XSACR operated in its nominal 10-minute scanning sequence during a stratiform
323 rain event observed on 11 August 2022, between 01-04 UTC (Fig. 4). The radars were exposed to
324 persistent rainfall, ranging from 1 mm hr^{-1} at 01 UTC to over 5 mm hr^{-1} around 02:15 UTC, leading
325 to strong radar signal attenuation, particularly visible in the KAZR Ze vertical gradient above 4
326 km (Fig. 4a). After 03 UTC, the surface rain intensity was so low that the disdrometer could not
327 effectively measure rain drop size distributions (DSDs) for Ze estimates due to insufficient drop
328 counts (< 20 drops/minute) (Fig. 4b).

329 The disdrometer-estimated surface Ze at Ka- (black diamonds) and X-bands (blue
330 diamonds) in Fig. 4c consistently show values close to 30 dBZ when rain rates are near 1 mm hr^{-1} ,
331 while the KAZR Ze is around 15 dBZ, resulting in a Dze of 15 dB against the disdrometer, as
332 shown in Fig. 4d. During this event, there is an 8-minute gap in every 2 minutes of VPT
333 measurements due to the PPI and HSRHI scans. The collocation of the 2-minute VPT data is
334 extended to a 6-minute window by averaging KaSACR/XSACR and VDISQUANTS data over a
335 ± 2 -minute interval.

336 The KaSACR Ze values (red crosses) in Fig. 4c display a sawtooth pattern within each 10-
337 minute scanning cycle. Each cycle begins with Ze values close to the XSACR Ze, followed by a
338 decline towards the KAZR Ze value as time progresses, with the scaling possibly related to the
339 rain rate. In contrast, the 03-04 September 2022 case in Fig. 2b shows parallel Ze trends between
340 the KAZR and KaSACR. The increasing Dze trend in each 6-minute period (red crosses) in Fig.
341 4d is more pronounced, indicating that the sawtooth behavior in KaSACR Ze and Dze results from
342 rainwater accumulation on the radome during the 2 minutes of vertical pointing. If the KaSACR
343 signal were saturating, it would consistently remain saturated rather than fluctuating. A closer
344 examination of XSACR Ze and Dze trends (black crosses) in Fig. 4c and d reveals minimal

345 variability with rain rates across the scanning cycle, likely due to the weaker water absorption
346 coefficient at X-band and the reduced water accumulation on the conical XSACR radome.

347 The differing KaSACR patterns between the events in Figures 2 and 4 are associated with
348 rainwater accumulation and the KaSACR/XSACR radar's cycling between scanning and
349 stationary VPT modes. At the start of each scanning VPT period, the radome is covered by a
350 relatively thin film of rainwater, having shed water during the RHI and PPI scans. In VPT mode,
351 excess rainwater rapidly accumulates on the radome, causing increased attenuation. Consequently,
352 WRA for the KaSACR is modulated by the 10-minute scanning cycle. By contrast, during the
353 continuous stationary VPT observations of KAZR and KaSACR on 03-04 September, rainwater
354 accumulated steadily on their radomes, resulting in similar WRA patterns, and the measured Z_e
355 and Dze were parallel with a consistent offset of approximately 7 dB.

356

357 3.3 WRA Fitting Calibration Technique

358

359 In this section, we examine the WRA behavior toward developing a relative calibration
360 technique for cloud radar monitoring. Figure 5a shows the estimated Z_e by KaSACR at 500 m
361 (black cross) after gaseous and rain attenuation corrections and the corresponding VDISQUANTS-
362 estimated Z_e (red cross) as a function of R for the 03-04 September case. A very well-correlated
363 monotonic relationship between the VDISQUANTS-estimated Z_e and R in logarithmic space is
364 observed. However, the KaSACR-measured Z_e is biased low relative to the estimated Z_e , and the
365 offset ($Dze = Z_{e_{dis}} - Z_{e_{meas}}$ shown in Fig. 5b) with increasing R . The Dze approaches 0 dB at
366 $R < 0.1 \text{ mm hr}^{-1}$, when minimal WRA is expected due to the limited water on the radome.
367 However, Dze increases up to 15 dB at $R \sim 5 \text{ mm hr}^{-1}$, which is potentially a disadvantage when
368 considering cloud radar observations in precipitation. However, this characteristic range of WRA
369 relative to R provides an opportunity for exploring relative radar calibration techniques.

370 Given a quasi-linear correlation between Dze and R in logarithmic space in Fig. 5b, a
371 weighted linear least-squares fit of the Dze with R in logarithm can be applied, as described in
372 Equation 2:

373

$$374 \quad Dze = a + b \log(R) \quad (2)$$

375 For the cases shown in Fig. 5b, the fitted slope b is estimated to be 8.6. The intercept " a " captures
376 the radar calibration offset and the WRA when R is 1 mm hr^{-1} . Given the KaSACR calibration

377 offset is close to 0, the intercept primarily reflects WRA at this rain rate, yielding an intercept of
378 approximately 11.1 dB.

379 This log-linear relation between Dze and R is different from the $R^{1/3}$ dependence described
380 by Gibble's formula (Eq.1), which is applied by Frasier et al. (2013) and Gorgucci et al. (2013) in
381 X-band radar calibrations. Since the water absorption coefficient at Ka-band is approximately three
382 times that at X-band, we divide the result of Eq. 2 by 3 and compare it with the fitting relations
383 from Frasier et al. (2013, solid blue line) and Gorgucci et al. (2013, solid black line) in Figure 6.
384 It is important to note that the X-band radars used in the studies by Frasier et al. (2013) and
385 Gorgucci et al. (2013) were equipped with spherical radomes, whereas the ARM KAZR and
386 KaSACR radars used flat inclined radomes. Despite these differences, the relationship derived in
387 this study intersects, with those of Frasier et al. (2013) and Gorgucci et al. (2013) at $R=0.2$ mm hr⁻¹,
388 aligning with the majority of our data. When $R > 0.2$ mm hr⁻¹, our WRA fitting results exceed
389 those of Gorgucci et al. (2013) by less than 0.5 dB, although Gorgucci et al.'s relation is 0.5-1 dB
390 higher than that of Frasier et al. (2013). When $R < 0.2$ mm hr⁻¹, our WRA fitting result is 0.5-1 dB
391 lower than both previous studies. The observed differences (within 1 dB) are smaller than the data
392 scatter in Fig. 5b (standard deviation of 3 dB) and the discrepancies between the two previous
393 studies, suggesting that the log-linear fitting in Eq. 2 is suitable for WRA correction when R is
394 below 5 mm hr⁻¹, the selected threshold for our analysis. The calibration offset calculation
395 associated with the WRA fitting functions will be further examined in Section 4.

396
397 Assuming that radar calibration offsets are independent of R , and that WRA depends
398 intrinsically on R , the radar calibration offset can be determined by monitoring the fitted intercept
399 in Eq. 2. Figure 5e shows the fitted intercept of Dze of KAZR is 18.5 dB, about 7.5 dB higher than
400 that of KaSACR, which is consistent with the observed offset between KaSACR and KAZR in
401 Figure 1d and the time series in Figure 2c. Alternatively, we can also assume negligible WRA at
402 very low rain rates, e.g., $R = 0.05$ mm hr⁻¹, making $Dze (R = 0.05)$ a reliable measure of the radar
403 calibration offset (C) for monitoring radar performance. For the KaSACR on 03-04 September
404 case (Fig. 5a), the $Dze (R=0.05)$ is -0.1 dB, while for the KAZR, it is 7.3 dB, consistent with direct
405 comparisons between KaSACR, KAZR, and VDISQUANTS. This finding suggests that the WRA
406 technique provides robust offset estimates for this case. The corrected Ze values using the log-
407 linear fitted Dze in Eq. 2 are compared with VDISQUANTS Ze in Fig. 5c and 5f for KaSACR and

Deleted: .

Deleted: The relationship from this study intersects

410 KAZR, respectively. The correlation coefficient (rr) improves to ~ 0.9 , with a mean bias of 0 dB
411 and a standard deviation of 3.0 dB for both KaSACR and KAZR.

412
413 To further explore the intrinsic WRA dependence on R , we applied the WRA log-linear
414 fitting calibration technique to KaSACR in its scanning-VPT modes. Due to water shedding during
415 the scanning cycle, we used the last-minute measurement of each 2-minute VPT period within the
416 10-minute scanning cycle. To obtain a range of samples, we identified five stratiform rain days—
417 May 25, August 5, 11, 19, and 29—and combined data from these events. The data collected from
418 those five days are plotted along with the corresponding VDISQUANTS-estimated Z_e (red cross)
419 as a function of rain rates in Fig. 5g. For these events, $Dze_{(R=0.05)}$ is -0.9 dB, with slope “b” fitted
420 to 8.6. The corrected Z_e using this log-linear fitted Dze is compared with the VDISQUANTS Z_e
421 in Fig. 7i, demonstrating a strong correlation with the reference Z_e , along with a smaller standard
422 deviation ($rr=0.91$; mean bias, 0 dB; and standard deviation, 2.0 dB).

423 Recall the $Dze_{(R=0.05)}$ of -0.1 dB for stationary VPT mode in 03-04 September case, the
424 difference between the two KaSACR offsets is less than 1 dB, which is well within the standard
425 deviation of the estimated Z_e (3 dB) as a function of R , and aligns closely with the 1 dB offset
426 from the direct disdrometer comparison at light rain onset in Fig. 2. This suggests that the R
427 dependence of WRA is a valid assumption, therefore the interceptor or $Dze_{(R=0.05)}$ in the fitting of
428 Eq. 2 can be a useful metric for radar offset monitoring.

429 The time and height plots of Z_e from KaSACR, XSACR, and KAZR GE and MD modes
430 on 03-04 September 2022 (after the WRA correction is applied) are shown in Figure 7. For the
431 precipitating period, KaSACR is adjusted with Eq. 2 with a slope of 8.6 and constant of 11.1 (Table
432 2 or Fig. 5b). XSACR is modified with the offset of 3 dB from VDISQUANTS (black cross in Fig
433 2d), and KAZR GE mode is corrected using Eq. 2 with a slope of 8.6 and an intercept of 18.5
434 (Table 2, or Fig. 5b). For non-precipitating periods, the calibration offsets for KaSACR and
435 XSACR are assumed to be 0 dB based on the previous discussion, while the KAZR GE mode is
436 calibrated with an offset of 7 dB. In contrast to the apparent difference of more than 5 dB between
437 KAZR and KaSACR shown in Figure 1, the corrected Z_e values from KAZR and KaSACR are
438 comparable to those from XSACR in cloud and light rain conditions. Under the relatively heavy
439 rain conditions (e.g., 2330 UTC), XSACR Z_e along the fall streaks maintains magnitudes near 30
440 dBZ from the surface up to the melting layer, while Z_e estimates from KAZR and KaSACR

441 gradually decrease from the surface to the melting layer, likely due to increasing attenuation in
442 Ka-band observations. This comparison in Figure 7 further supports the applicability of the WRA
443 fitting technique to KAZR measurements and KaSACR in VPT modes, providing reasonable
444 estimates for wet-radome corrections during precipitation and radar offset monitoring.

445

446 4 Application and Evaluation of the WRA Offset Monitoring During TRACER

447 4.1 Daily TRACER KAZR Calibration Offset Applications

448

449 We apply the WRA fitting technique on the Dze and R relationship using VDISQUANTS
450 Ze estimates versus KAZR Ze for each day with measured precipitation throughout TRACER
451 campaign. The fitted slopes from the daily events typically range from 6 to 10, with rr generally
452 exceeding 0.7. The fitted slopes and associated fitting errors depend on the distribution of data
453 samples. For example, in rain events with short durations or limited variability in intensity, data
454 samples may cluster within a narrower range, resulting a relatively lower correlation coefficient
455 between the fitted Ze and disdrometer Ze , potentially indicating less reliable results.

456

457 To mitigate uncertainty associated with “daily” fitting as above, one may assume that the
458 Dze and R relation has a constant slope over longer windows. In this study we consider applying
459 the WRA fitting technique with an average slope of 8, selected as a representative value for
460 extended rain conditions across the entire TRACER campaign dataset. As a sensitivity study of
461 this composite slope, we conduct offset calculations with proxy slope values at 6, 8 and 10 for both
462 KAZR and KaSACR in the 03-04 September 2022 case. Table 2 presents the results of these tests.
463 As the slopes increase from 6 to 10, the calibration offsets for both KAZR and KaSACR decrease
464 by approximately 3 dB, as expected. With increasing slope values, the least-squares fit prioritizes
465 the data samples around 0.1 - 1 mm hr⁻¹, resulting in a mathematical decrease in C .

466 To further illustrate, we applied the WRA fitting with a slope of 6 to the KaSACR
467 observations in Figure 5a. The fitted relation is represented by the red dashed line in Figure 6. It
468 can be seen that the fitted Ze with a slope of 6 lies between the results from Frasier et al. (2013)
469 and Gorgucci et al. (2013). For most data samples (concentrated around 0.1 - 1 mm hr⁻¹), the
470 difference between the two WRA fitting results remains within 1 dB. The resulting C with slope
471 of 6 is larger than that with a slope of 8. However, the offset deviation due to possible fitting slope
472 fitting changes (shown in Table 2) is 3 dB, which is within the standard deviation of the estimated

473 Z_e as a function of R (~ 3 dB). Therefore, even with fitting slope errors associated with this relative
474 WRA technique, drifts larger than the 3 dB in the long-term calibration trend would be meaningful
475 and identifiable.

476 The calculated KAZR calibration offsets during the entire TRACER campaign are shown
477 in Fig. 8a (black asterisk for the daily value, thin dash line representing the mean campaign-wide
478 trend). The calibration offsets remain relatively stable around 2 dB, with a standard deviation of 3
479 dB until 1 July 2022 (273 days since 1 Oct. 2021 in Fig. 8). After this date, the calibration offset
480 increases to around 7 dB in September. This shift is larger than the uncertainty of the fitting method
481 and the standard deviation of the fitting data, which is found to be linked to a drop of about 1 dB
482 in transmitter power toward the end of the project in TRACER radar b1 data processing (Feng et
483 al., 2024) and in Figure 9c.

484
485

486 4.2 Evaluation of the TRACER KAZR Calibration Trend

487 By monitoring the $Dze_{(R=0.05)}$ from each rainy day that meets our stratiform and duration
488 selection criteria, we determine a relative radar calibration offset trend. This offset includes
489 additional uncertainty due to fitting uncertainty and the assumption of negligible WRA at $R \sim 0.05$
490 mm hr^{-1} . Combining this WRA fitting technique with other, typically less frequent, absolute radar
491 calibration references would be ideal and cost-effective for KAZR long-term calibration. To
492 evaluate the KAZR calibration offset trend over the entire TRACER campaign, we performed
493 three separate tests to demonstrate the potential offset uncertainty and/or advantages of the current
494 WRA fitting technique compared to other established methods.

495

496 4.2.1 Direct KAZR-Disdrometer Comparison Near to Light Rain Onset

497 As previously noted, a wet radome film may not form immediately at the onset of light
498 rain, so WRA is often assumed to be negligible when calibrating radar using disdrometer
499 measurements near these rain onset windows. We perform a direct KAZR-disdrometer comparison
500 at or near light rain onset for qualifying KAZR calibration events. The onset mean offset for each
501 day is calculated if there are data samples with $R < 0.1 \text{ mm hr}^{-1}$ lasting for 5 consecutive minutes
502 within each observed rain event. The onset mean offsets are shown in Fig. 8a (red diamonds). For
503 days with an onset mean offset, these values are typically close to those calculated using the WRA

504 fitting technique. However, this method’s applicability depends on the variation in precipitation
505 rate over the 5-minute sampling period and the minimum sensitivity of VDISQUANTS. The
506 former introduces large uncertainty, while the latter limits the number of data samples, as shown
507 in Fig. 8a.

508

509 *4.2.2 WRA Fitting Technique Against the Calibrated RWP Z_e*

510 As an independent cross-comparison, we also apply the WRA fitting technique with respect
511 to calibrated RWP Z_e at RWP time resolution (less than 8 seconds), using interpolated disdrometer
512 rain rates over the entire TRACER campaign. Here, Dze is replaced by the difference between
513 KAZR and RWP measurements. The WRA calibration offsets using RWP measurements are
514 shown with black asterisks in Fig. 8b. First, we observe fewer available RWP data points, due to
515 RWP mode switching during transient rain events. For days with available RWP measurements,
516 the calibration offsets closely align with those derived using disdrometer-estimated Z_e in Fig. 8a
517 and direct disdrometer comparisons. The offset trend drift from early July to September is
518 smoother and more clearly defined than the trend observed with disdrometer measurements, likely
519 due to better temporal resolution. Overall, the consistency in temporal trend and magnitude of
520 calibration offsets between disdrometer and RWP measurements indicates strong performance of
521 the new WRA fitting technique.

522

523 *4.2.3 Cross-Comparison Between KaSACR and KAZR*

524 As previously mentioned, KaSACR calibration offsets remained stable between May and
525 September 2022. Furthermore, its calibration offsets, calculated from the WRA fitting technique
526 with scanning VPT and stationary VPT measurements in Fig. 6, are approximately -0.9 to -0.1 dB,
527 respectively, and around 1 dB from direct disdrometer comparison at light rain onset. We
528 tentatively assign a calibration offset of 0 dB for KaSACR observations. Cross-comparison
529 between KaSACR VPT mode and KAZR observations can then be used to quantify the KAZR
530 calibration offset trend. Since KaSACR and KAZR operate at the same frequency, this cross-
531 comparison uses full-profile samples rather than measurements at a specific height level, as
532 cumulative gaseous and rain attenuation should be consistent across range gates.

533 For this cross-comparison, we first match the closest KaSACR profiles to KAZR profiles
534 and interpolate KaSACR height ranges to align with KAZR height ranges. We then select data

535 samples using a signal-to-noise ratio threshold of 5 dB for both KaSACR and KAZR. In
536 precipitating events, KaSACR in scanning VPT mode is expected to exhibit a sawtooth or
537 modulated WRA cycling behavior, while KAZR VPT operates under consistent/continuous WRA
538 (see Fig. 2). We categorize the collocated profiles into precipitating and non-precipitating periods
539 using collocated surface rain rates from disdrometer measurements. Finally, the daily mean offsets
540 between KaSACR and KAZR observations in non-precipitating clouds are calculated and shown
541 in Fig. 8b (red diamonds). These calculated offsets display a trend similar to that observed from
542 the WRA fitting technique against RWP measurements in Fig. 8b, further supporting the validity
543 of the WRA calibration offset behaviors and strengthening confidence in the offset drift observed
544 at the end of the campaign.

545 To extend the method to different disdrometer setups, we applied the WRA fitting
546 technique to LDQUANTS estimates. Additionally, we tested sensitivity to fitting functions of log-
547 linear and $R^{1/3}$ dependencies to account for potential discrepancies. Figures 9a and 9b present the
548 results with a 2-day running average. The daily calibration offsets show slight variations between
549 LDQUANTS and VDISQUANTS, indicating minor differences in disdrometer measurements
550 (Wang et al. 2021). While the calibration offsets from the log-linear and $R^{1/3}$ fittings can differ by
551 up to 2 dB for certain day, the overall trends remain similar, with a mean offset of approximately
552 2 dB before July 2022, increasing to around 7 dB afterward. The increase of calibration offsets is
553 well correlated with the noticeable decrease of transmitted power (Figure 9c) observed at the end
554 of the project.

555 5 Summary

556 In this study, we have demonstrated the wet radome influence on Ka-band radar
557 observations through comparisons that included KaSACR VPT observations under scanning (that
558 may shed water buildup) and stationary (non-shedding) conditions. The WRA is attributed to both
559 wet film and cumulative rainwater collecting on the radar radome. This attenuation influence
560 increases, as the rain rate increases. In campaign settings, it was found this attenuation may exceed
561 10 dB under a modest rain rate of 5 mm hr^{-1} . Taking advantage of the intrinsic WRA dependence
562 on rain rates as obtained in moderate rain events from the AMF1 deployment in Houston, TX

563 during the TRACER field campaign, a new relative calibration monitoring technique was
564 developed for use with the ARM KAZR (or similar cloud radar systems) observations.

565 The well-correlated relation between Dze and R (in logarithmic space) on precipitating
566 days is fitted with a log-linear equation. This rain dependence of WRA serves as the basis for this
567 relative WRA calibration technique. The corrected KAZR Ze with fitted Dze , which includes the
568 WRA and Ze offset, agrees very well with both disdrometer-estimated and RWP-measured Ze .
569 The radar calibration offset is calculated from the fitted Dze - R relation when R equals 0.05 mm
570 hr^{-1} , assuming WRA is negligible at this light rain rate. The daily fitted slopes over the course of
571 the TRACER campaign vary between 6 and 10 due to different data sampling in different rain
572 types. A slope sensitivity study suggests that the calibration offset deviations due to slope variation
573 are likely within the standard deviation of the estimated Ze as function of R , as well as those typical
574 of underlying/collocated disdrometer measurement uncertainty (i.e. $\sim 2\text{-}3 \text{ dB}$). The KAZR
575 calibration offsets calculated with a constant slope of 8 during the TRACER campaign are stable
576 near 2 dB compared to the disdrometer estimate with a standard deviation of 3 dB through June
577 2022. After that time, the calibration offsets increase to more than 7 dB.

578 The performance of the WRA fitting calibration technique is evaluated by comparing it
579 with direct disdrometer measurements at the onset of rain events. The wet-radome technique
580 consistently identifies a sound calibration offset over the entire project and arguably outperforms
581 the direct disdrometer and radar comparison at the onset of light rain by reducing noise and
582 increasing temporal consistency. The WRA fitting calibration technique is also applied to the
583 KAZR observation against the calibrated RWP Ze reference. This test reveals sound performance
584 and a clear and smooth matching trend in the July to September change in TRACER KAZR offsets,
585 indicating that the new technique can be applicable to other calibrated reference radars with
586 collocated surface rain rate measurements. The KAZR offset assessed from the cross-comparison
587 between the stable and calibrated KaSACR VPT mode and KAZR observations in non-
588 precipitating clouds also agree with the calibration offset trend from the WRA fitting technique.
589 The daily calibration offsets vary due to the uncertainty of disdrometer measurements and the
590 fitting function of WRA, however the generally long-term trend from the WRA fitting technique
591 seems robust.

592

593 Determining the calibration offset and monitoring the long-term trend of ARM KAZR is
594 the first step towards studying cloud seasonal and inter-seasonal variation. Having an easily
595 adjustable cloud radar calibration method with collocated disdrometer or RWP data available will
596 also facilitate cloud microphysical property retrieval, cloud process studies, and cloud variation
597 associated with climate change using ARM KAZR measurements. This technique has the
598 advantage of utilizing data from a broader range of light and moderate rain cases, avoiding the
599 stringent requirements of other shorter-wavelength radar monitoring methods, which often rely on
600 disdrometers or other radars and require observations of cloud, drizzle, or light rain at the onset of
601 precipitation. Future plans include testing this newly developed WRA technique at other ARM
602 fixed sites (e.g., in more humid, marine, or oceanic environments) to assess the extent of any
603 necessary site-specific refinements for different radars and sampling conditions, acknowledging
604 that wet-radome attenuation is inherently dependent on both the radome and radar characteristics.
605 Recently, this WRA monitoring technique has been applied to data from other ARM field
606 campaigns, such as the Surface Atmosphere Integrated Field Laboratory (SAIL) and the Eastern
607 Pacific Cloud Aerosol Precipitation Experiment (EPCAPE). Alongside TRACER, the offset trends
608 derived from these three campaigns have shown favorable agreement with results from other
609 independent KAZR calibration techniques documented in ARM radar b1 data processing reports
610 (Feng et al., 2024; Matthew et al., 2024; Rocque et al., 2024).

611
612
613
614
615
616
617
618
619
620
621
622
623

Deleted:

Deleted: .

626 Table 1. List of parameters for KAZR GE mode, KaSACR/XSACR in vertical pointing (VPT)
 627 mode, and RWP in precipitation mode.

Deleted: ¶
 ¶
 ¶

| | KAZR (GE mode) | KaSACR (VPT mode) | XSACR (VPT mode) | RWP (Precipitation mode) |
|-------------------------|----------------------|----------------------|---------------------|--------------------------------|
| Frequency (GHz) | 34.0 | 35.3 | 9.71 | 1.29 |
| Wavelength | 8.57mm | 8.50mm | 3.09cm | 23.3cm |
| Beam width (degree) | 0.3 | 0.3 | 1.0 | >3 |
| Time resolution (s) | 2 | 4 | 3 | 5-8 |
| Range resolution (m) | 30 | 25 | 25 | 225 |
| Minimum range (m) | 160 | Others: 428 | 288 | 335 |
| | | 0903/04: 453 | | |
| Radome diameter (m) | 1.82 | 1.82 | 1.82 | N/A |

629
 630
 631
 632
 633
 634
 635
 636
 637
 638
 639
 640
 641
 642
 643
 644
 645
 646
 647
 648
 649
 650
 651

656 Table 2. Sensitivity study of the slope value in the log-linear fitting for KAZR and KaSACR
 657 calibration on 03-04 September 2022 case in Figure 1. b and a are the slope and constant,
 658 respectively, in the log-linear fitting in Eq. 2. $D_{Ze}(R=0.05)$ is the radar calibration offset when rain
 659 rate (R) equals 0.05 mm hr^{-1} . More details can be found in Section 3.3.

660

| b | KAZR | | | | KaSACR | | | |
|-----|------|--------------------------|--|-------------------------------|--------|--------------------------|--|-------------------------------|
| | a | D_{Ze} ($R=0.05$) | Correlation coefficient (rr) | Standard deviation (dB) | a | D_{Ze} ($R=0.05$) | Correlation coefficient (rr) | Standard deviation (dB) |
| 6 | 17.1 | 9.3 | 0.88 | 3.8 | 9.8 | 2.0 | 0.89 | 3.4 |
| 8 | 18.1 | 7.7 | 0.90 | 3.9 | 10.9 | 0.5 | 0.91 | 3.4 |
| 8.6 | 18.5 | 7.3 | 0.91 | 4.1 | 11.1 | -0.1 | 0.92 | 3.5 |
| 10 | 19.1 | 6.3 | 0.92 | 4.4 | 12.0 | -1.0 | 0.93 | 3.7 |

661

662

663

664

665

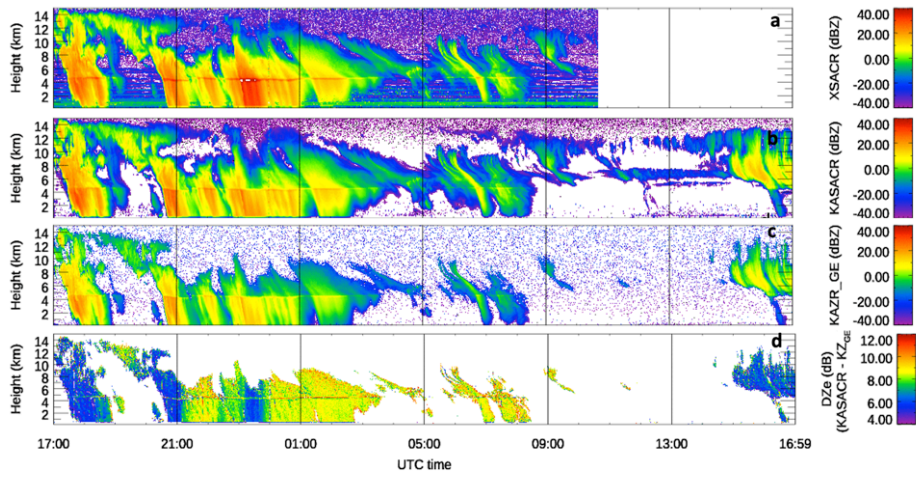
666

667

668

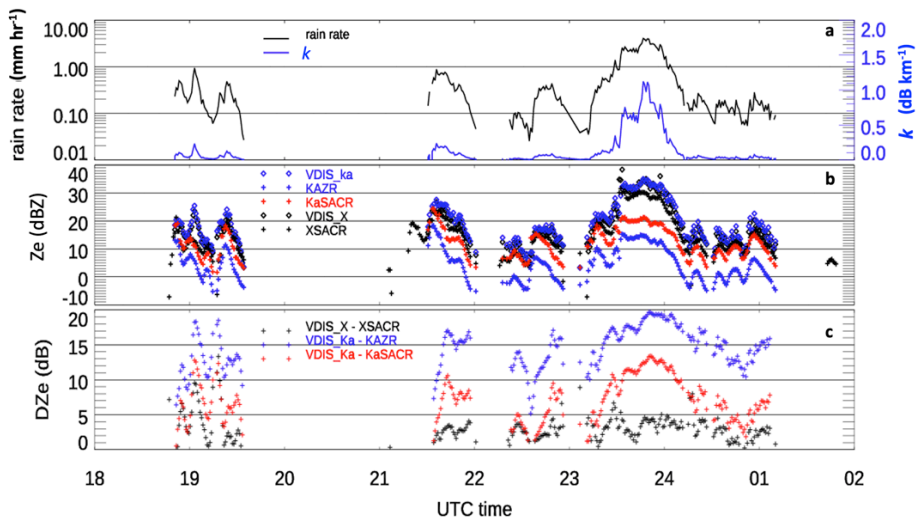
669

670



671
 672 Figure 1. Measured radar reflectivity on 03-04 September 2022 from the TRACER field campaign.
 673 a) XSACR, missing data after 10:40 UTC on 04 September 2022, b) KaSACR, c) KAZR GE mode,
 674 d) Ze difference (DZe) between the KaSACR and the KAZR GE mode.

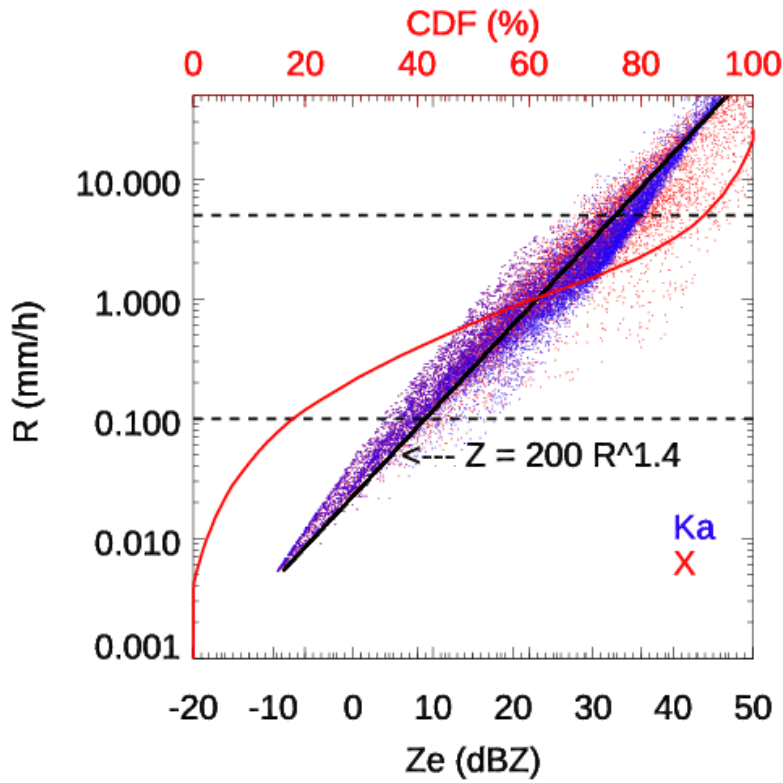
675
 676
 677
 678
 679
 680



681
 682
 683 Figure 2. Measurements and comparison on 03-04 September 2022 between VDISQUANTS and
 684 radars. a) the timeseries of VDISQUANTS rain rate (black line) and rain droplet specific
 685 attenuation coefficients (K , blue line) at Ka band. b) the time series of measured Z_e from KAZR
 686 GE (blue +), KaSACR (red +), and XSACR (black +) at 500 m after gaseous and rain attenuation
 687 corrections, and estimated Z_e from VDISQUANTS at Ka (blue diamond) and X (black diamond)
 688 bands. c) Z_e difference (DZe) between radar and disdrometer for XSACR (black cross), KaSACR
 689 (read cross), and KAZR (blue cross). For this case, SACR was operated in the stationary VPT
 690 mode.

691
 692
 693
 694
 695
 696
 697
 698
 699
 700
 701
 702
 703
 704

705



706

707 Figure 3. The estimated Ze from VDISQUANTS for Ka (red dots) and X bands (black dots) during
 708 the entire TRACER campaign, plotted as a function of rain rate (R). The red line is the cumulative
 709 probability function (CDF) of R . The two vertical black lines are at rain rates of 0.1 and 5.0 mm
 710 hr^{-1} , respectively. The Z-R relation is fitted in black line with $Z=200R^{1.4}$, which is slightly smaller
 711 than the WSR-88D Z-R relation in convective summer deep convection ($Z = 300R^{1.4}$, Crosson,
 712 1996)

713

Deleted:

Deleted: blue

Formatted: Font: Italic

Formatted: Font: Italic

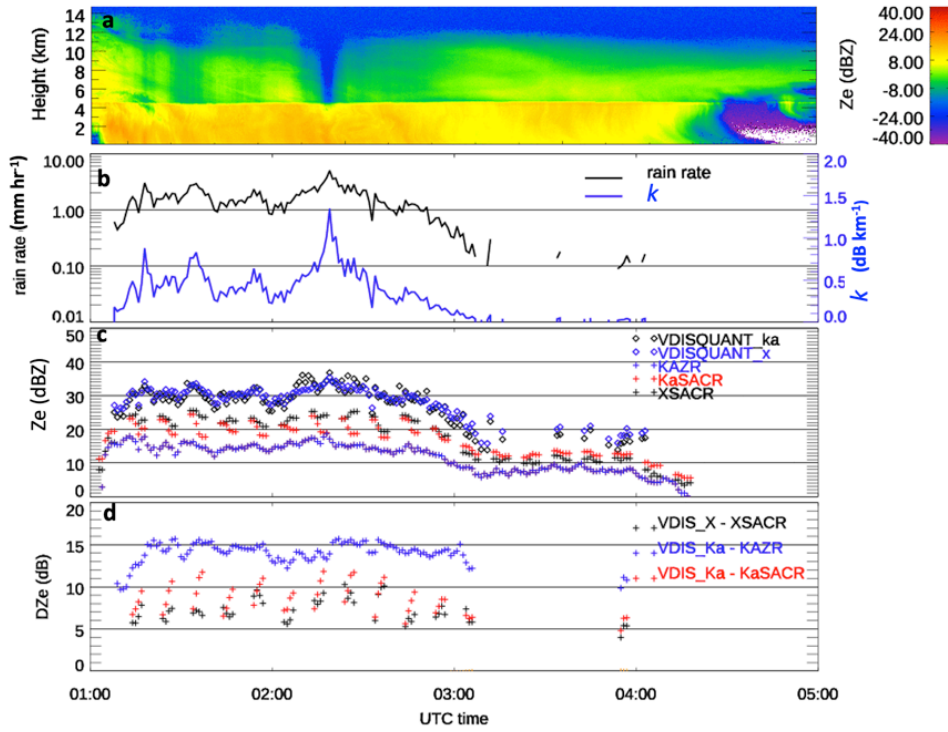
Formatted: Superscript

Formatted: Font: Italic

Formatted: Font: Italic

Formatted: Superscript

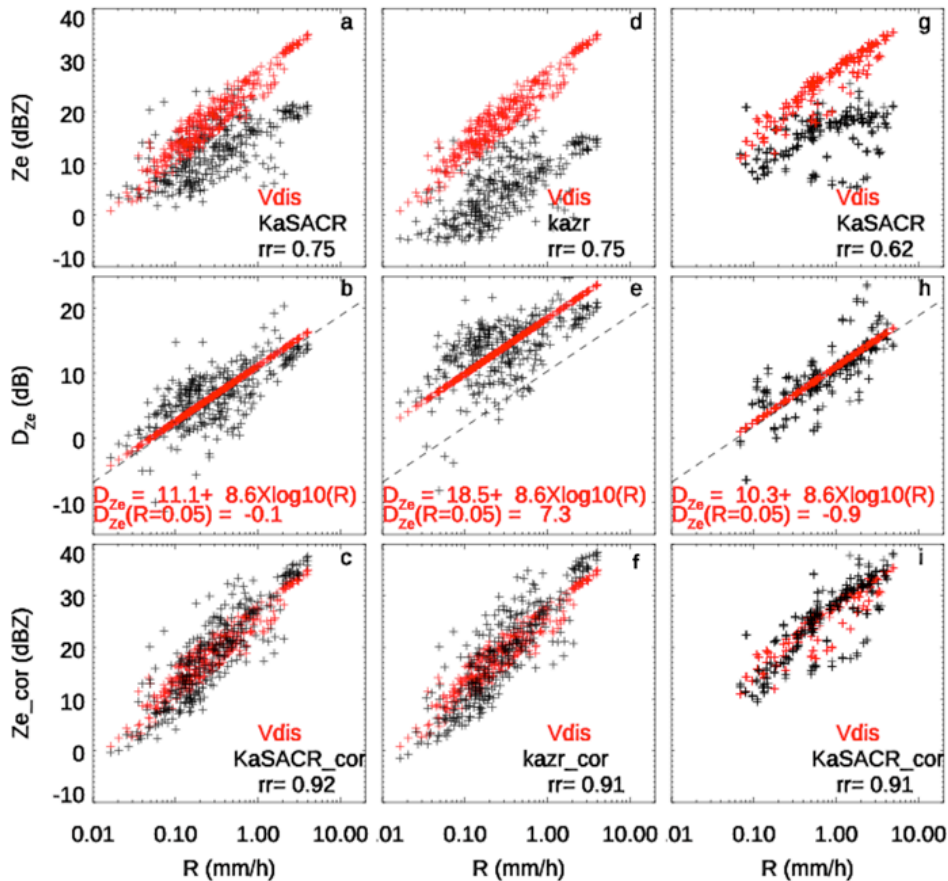
Deleted: ¶



717

718 Figure 4. Radar and VDISQUANTS comparison for the case on August 11. a) Measured radar
 719 reflectivity (Z_e) from the KAZR GE mode. b-d are similar to Fig. 2a-c. For this case, KaSACR
 720 and XSACR measurements are the scanning VPT mode and collocated with the VDISQUANTS
 721 with a ± 2 minutes averaging window.

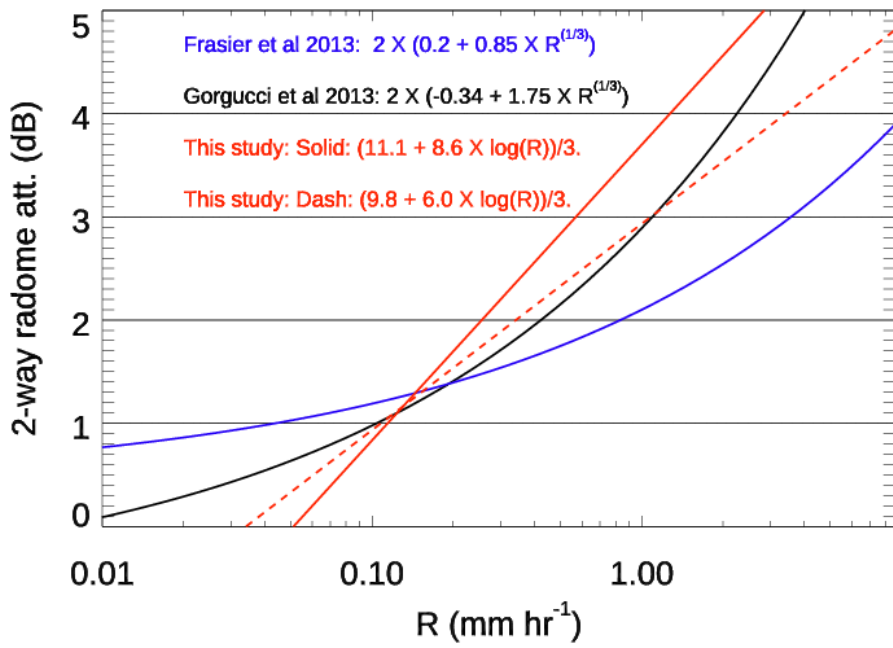
722



723

724 Figure 5. a) Scatter plot of radar measured Z_e (black cross) at 500 m and VDISQUANTS-estimated
 725 Z_e (red cross) as a function of rain rate R , b) Difference between measured Z_e and VDISQUANTS-
 726 estimated Z_e (D_{ze} in black). The log-linear fitting in Eq. 2 with slope b at 8.6 are plotted in red
 727 cross, c) Scatter plot of radar measured Z_e (black cross) after log-linear fitting correction along
 728 with the VDISQUANTS-estimated Z_e (red cross) for KaSACR stationary VPT (a-c) and KAZR
 729 GE (d-f) on 03-04 September, and KaSACR stationary VPT (g-i) collected on May 25, August 05,
 730 11, 19 and 29. The correlation coefficients between the measured Z_e and estimated Z_e (rr) before
 731 and after the fitting correction are noted. The dashed black lines in second row (b, e, h) are the log-
 732 linear fitting with $a=10.3$ and $b=8.6$ for KaSACR in Table 2.

733
734
735
736



737

738 Figure 6. Two-way radome attenuation as a function of rain rate (R) using the log-linear WRA
739 fitting relation in Eq. 2 with slopes of 8.6 (solid red) and 6.0 (dashed red) in this study at Ka-band,
740 which is divided by 3 and compared with two previous studies about X-band radars from Frasier
741 et al. 2013 and Gorgucci et al. 2013.

742

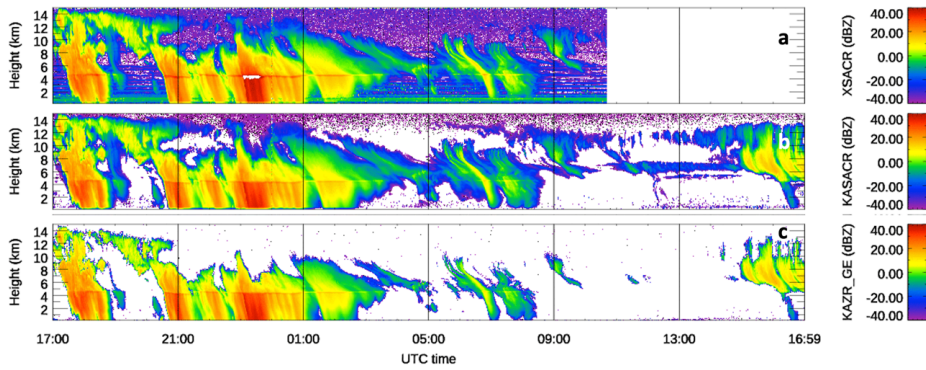
743

744

745

746

747



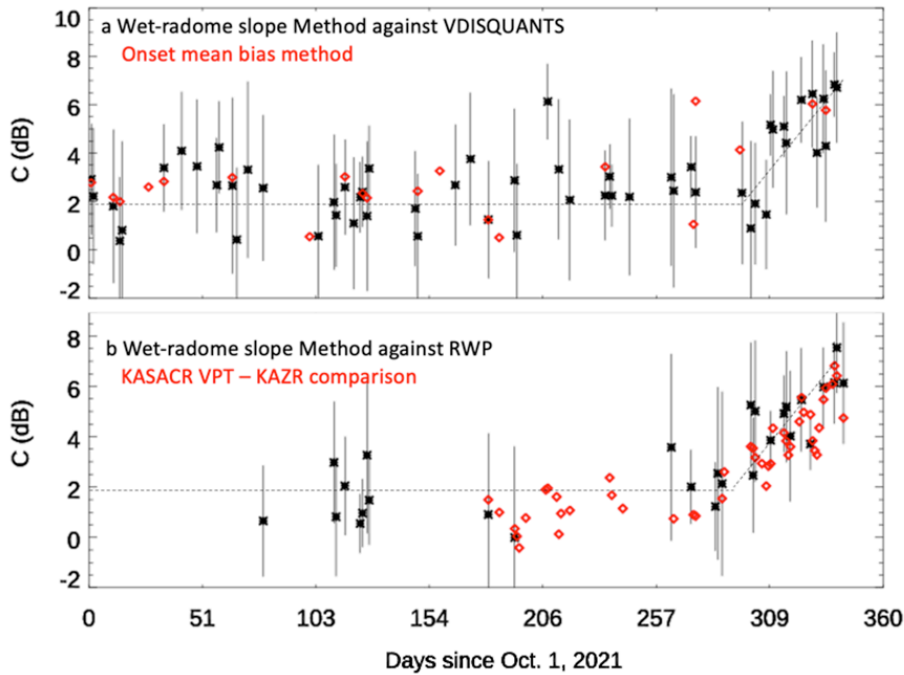
748

749 Figure 7. The same as Figure 1a-c except after WRA correction and radar calibration. For the
750 precipitating period, KaSACR is corrected using Eq. 2, with a slope of 8.6 and constant of 11.1.
751 XSACR is corrected with the offset of 3 dB from VDISQUANTS (black cross in Fig 2d), and
752 KAZR GE mode is corrected using Eq. 2, with a slope of 8.6 and constant of 18.5. For non-
753 precipitating periods, the calibration offsets of KaSACR and XSACR are assumed to be 0 dB,
754 while the KAZR GE mode is calibrated with offset of 7 dB.

755

756

757

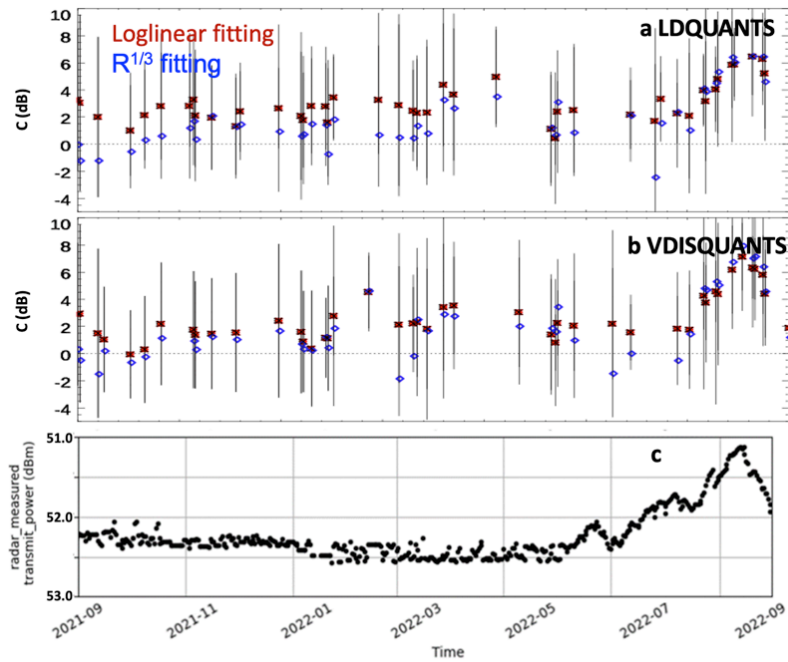


758
 759
 760 Figure 8. a) KAZR daily calibration offsets (C) from the mean KAZR bias method at the onset of
 761 light rain (red diamond) and the WRA fitting technique (black asterisk) against the VDISQUANTS
 762 data. Black vertical bar is the standard deviation of corrected Z_e against the estimated Z_e . b) KAZR
 763 daily calibration offset from the WRA fitting technique against the calibrated RWP measurement
 764 in black asterisk with vertical standard deviation bar. Red diamonds stand for the daily cross-
 765 comparison between the KaSACR VPT mode and the KAZR GE mode in non-precipitating clouds
 766 since May 26, 2022. The dashed black line is the mean trend outline from the WRA fitting
 767 technique in Fig. 8a.

768

769

770



771

772 Figure 9 KAZR daily calibration offsets (C) from log-linear fitting with Eq. 2 (red asterisk with
 773 black standard deviation bar) or the $R^{1/3}$ relation (blue diamond) against a) LDQUANTS and b)
 774 VDISQUANTS data. The daily offsets are smoothed with 2-day window. c) KAZR transmitted
 775 power. Noticeable decrease of transmitted power is well correlated with the increase of calibration
 776 offset.

777

778

779

780

781

782 Data availability

783
784 The KAZR, KaSACR and XSACR data at the TRACER campaign in this study are a1-level data.
785 The surface disdrometer VDISQUANTS and interpolated sounding data are c1-level value added
786 product data. They are all available at ARM data discovery at <https://adc.arm.gov/discovery/#/> and
787 through the following DOIs. The calibrated radar wind profiler data is ARM PI product and can
788 be obtained from the data developer, Dr. Christopher R. Williams, through email
789 (christopher.williams@colorado.edu) contact.

790
791 Bharadwaj, Nitin, Hardin, Joseph, Isom, Bradley, Johnson, Karen, Lindenmaier, Iosif, Matthews,
792 Alyssa, Nelson, Danny, Feng, Ya-Chien, Deng, Min, Rocque, Marquette, Castro, Vagner,
793 and Wendler, Tim. *Ka-Band Scanning ARM Cloud Radar*. United States: N. p., 2021. Web.
794 doi:10.5439/1469302.

795 Bharadwaj, Nitin, Hardin, Joseph, Isom, Bradley, Johnson, Karen, Lindenmaier, Iosif, Matthews,
796 Alyssa, Nelson, Danny, Feng, Ya-Chien, Deng, Min, Wendler, Tim, Castro, Vagner, and
797 Rocque, Marquette. *X-Band Scanning ARM Cloud Radar*. United States: N. p., 2021. Web.
798 doi:10.5439/1469303.

799 Hardin, Joseph, Giangrande, Scott, and Zhou, Aifang. *Idquants*. United States: N. p., 2019. Web.
800 doi:10.5439/1432694.

801 Hardin, Joesph, Giangrande, Scott, Fairless, Tami, and Zhou, Aifang. *vdisquants: Video*
802 *Distrometer derived radar equivalent quantities. Retrievals from the VDIS instrument*
803 *providing radar equivalent quantities, including dual polarization radar quantities (e.g.,*
804 *Z, Differential Reflectivity ZDR)*. United States: N. p., 2021. Web. doi:10.5439/1592683.

805 Isom, Bradley, Nelson, Danny, Andrei, Iosif, Hardin, Joseph, Matthews, Alyssa, Johnson, Karen,
806 Bharadwaj, Nitin, Feng, Ya-Chien, Rocque, Marquette, Deng, Min, Wendler, Tim, and
807 Castro, Vagner. *ARM: KAZRCFRGE*. United States: N. p., 2018. Web.
808 doi:10.5439/1498936.

809 Isom, Bradley, Nelson, Danny, Andrei, Iosif, Hardin, Joseph, Matthews, Alyssa, Johnson, Karen,
810 Bharadwaj, Nitin, Feng, Ya-Chien, Rocque, Marquette, Deng, Min, Wendler, Tim, and
811 Castro, Vagner. *ARM: KAZRCFRMD*. United States: N. p., 2018. Web.
812 doi:10.5439/1498948.

813 Jensen, Michael, Giangrande, Scott, Fairless, Tami, and Zhou, Aifang. *interpolatedsonde*. United
814 States: N. p., 1998. Web. doi:10.5439/1095316.

815
816
817
818
819
820
821
822
823
824
825
826
827
828
829
830
831
832
833
834
835
836
837
838
839
840
841
842
843

844 Author contribution

845 MD developed the main concept for the WRA calibration technique and led the manuscript
846 preparation. SG, MJ, and KJ contributed to the data analysis process. CW provided the
847 calibrated RWP data and contributed to its analysis and write-up. JC, YF, AM, MR, and
848 MD, as part of the ARM radar data mentor team, provided TRACER-related radar
849 information and additional KAZR calibration used in TRACER b1 data processing. IL and
850 TW, as ARM radar engineers, supplied critical information on radar hardware, software,
851 and radar saturation. AZ and DW contributed as the disdrometer mentors and VAP
852 developers. ZZ and EL provided valuable insights regarding radar wet radome attenuation.
853 All coauthors helped to edit and comment the manuscript draft.

854

855 Competing interests

856 The authors declare that they have no conflict of interest.

857

858

859

860

861

862

863

864

865

866

867

868

869

870

871

872

873

874 Acknowledgement

875
876 We acknowledge the exceptional work of the radar engineering team and data mentor team for the
877 close to 100% operation rate of KAZR during the TRACER campaign. We would like to thank
878 the ARM TRACER team for the quality data of KaSACR, XSACR, disdrometer, RWP and
879 interpolated sounding measurements. Contributions from Brookhaven National Laboratory co-
880 authors were supported by the Atmospheric Radiation Measurement (ARM) Facility and the
881 Atmospheric System Research (ASR) program of the Office of Biological and Environmental
882 Research in the U. S. Department of Energy, Office of Science, through Contract No. DE-
883 SC0012704. Dr. C.R. Williams and the RWP work is supported under ASR grant number DE-
884 SC0021345. Pacific Northwest National Laboratory (PNNL) is operated by Battelle for the U. S.
885 Department of Energ. The authors from PNNL are also supported by ARM through Contract
886 No. DE-SC0015990.

887

888 Reference

889 Anderson, I., 1975: Measurements of 20-GHz transmission through a radome in rain. *IEEE Trans.*
890 *Antennas Propag.*, 23, 619–622.

891 Baldini, L., V. Chandrasekar, and Dmitri Moisseev 2012: Microwave radar signatures of
892 precipitation from S band to Ka band: application to GPM mission, *International Journal*
893 *of Remote Sensing*, Volume 41, 2020 - Issue 13, <https://doi.org/10.5721/EuJRS20124508>

894 Bertie J. E.; Lan Z. (1996). "Infrared Intensities of Liquids XX: The Intensity of the OH Stretching
895 Band of Liquid Water Revisited, and the Best Current Values of the Optical Constants of
896 H₂O(l) at 25°C between 15,000 and 1 cm⁻¹". *Applied Spectroscopy*. 50 (8): 1047-
897 1057. doi:10.1366/0003702963905385. S2CID 97329854.

898 Bringi, V. N, V Chandrasekar, N Balakrishnan, and DS Znić. 1990. "An Examination of
899 Propagation Effects in Rainfall on Radar Measurements at Microwave Frequencies."
900 *Journal of Atmospheric and Oceanic Technologies* 7(6): 829–840,
901 [https://doi.org/10.1175/1520-0426\(1990\)0072.0.CO;2](https://doi.org/10.1175/1520-0426(1990)0072.0.CO;2)

902 Bringi, V. N., and Chandrasekar V., 2001: Polarimetric Doppler Weather Radar. Cambridge
903 University Press, 636 pp.

904 Bechini, R., V. Chandrasekar, R. Cremonini, and S. Lim, 2010: Radome attenuation at X-band
905 radar operations. Proc. Sixth European Conf. on Radar in Meteorology and Hydrology,
906 Sibiu, Romania, ERAD, P15.1.

907 Bringi, V. N, Kumar Vijay Mishra, Merhala Thurai, Patrick C. Kennedy, and Timothy H. Raupach
908 2020: Retrieval of Lower-Order Moments of the Drop Size Distribution using CSU-CHILL
909 X-band Polarimetric Radar: A Case Study. Atmospheric Measurement Techniques.
910 <https://doi.org/10.5194/amt-2020-160>

911 Chandrasekar, V, L Baldini, N Bharadwaj, and PL Smith. Recommended Calibration Procedures
912 for GPM Ground Validation Radars, 103.

913 [Crosson, W., Duchon, C., Raghavan, R., & Goodman, S. \(1996\). Assessment of Rainfall Estimates
914 Using a Standard Z-R Relationship and the Probability Matching Method Applied to
915 Composite Radar Data in Central Florida. *Journal of Applied Meteorology*, 35, 1203-
916 1219. \[https://doi.org/10.1175/1520-0450\\(1996\\)035<1203:AOREUA>2.0.CO;2\]\(https://doi.org/10.1175/1520-0450\(1996\)035<1203:AOREUA>2.0.CO;2\).](#)

917

918 Deng, M., and Pavlos Kollias, Zhe Feng, Chidong Zhang, Charles N. Long, Heike
919 Kalesse, Arunchandra Chandra, Vickal V. Kumar, and Alain Protat, 2014: Stratiform and
920 Convective Precipitation Observed by Multiple Radars during the DYNAMO/AMIE
921 Experiment. *J. Appl. Meteor. Climatol.*, 53, 2503–2523, <https://doi.org/10.1175/JAMC-D-13-0311.1>.

923 Feng, Y-C, A Matthews, M Rocque, M Deng, T Wendler, K Johnson, E Schuman, I Lindenmaier,
924 V Castro, SE Giangrande, S Collis, R Jackson, A Theisen, and J Comstock. 2024.
925 TRACER b1 Data Processing: Corrections, Calibrations, and Processing Report. U.S.
926 Department of Energy, Atmospheric Radiation Measurement user facility, Richland,
927 Washington. DOE/SC-ARM-TR-297.

Formatted: Indent: Left: 0", Hanging: 0.5", Space Before: 0 pt

Formatted: No underline

928 Frasier, S. J., F. Kabeche, J. Figueras i Ventura, H. Al-Sakka, P. Tabary, J. Beck, and O. Bousquet,
929 2013: In-Place Estimation of Wet Radome Attenuation at X Band. *J. Atmos. Oceanic*
930 *Technol.*, 30, 917–928, <https://doi.org/10.1175/JTECH-D-12-00148.1>.

931 Frech, M., Lange, B., Mammen, T., Seltmann, J., Morehead, C., & Rowan, J. (2013). Influence of
932 a Radome on Antenna Performance, *Journal of Atmospheric and Oceanic*
933 *Technology*, 30(2), 313-324. Retrieved Mar 6, 2023,
934 from https://journals.ametsoc.org/view/journals/atot/30/2/jtech-d-12-00033_1.xml

935 Gible, D., 1964: Effect of rain on transmission performance of a satellite communication system.
936 *IEEE International Convention Record, Part VI, IEEE*, 52.

937 Giangrande, S. E., and A. V. Ryzhkov, 2005: Calibration of Dual-Polarization Radar in the
938 Presence of Partial Beam Blockage. *J. Atmos. Oceanic Technol.*, 22, 1156–1166,
939 <https://doi.org/10.1175/JTECH1766.1>.

940 Giangrande, S. E., E. P. Luke and P. Kollias, 2010: Automated retrievals of precipitation
941 parameters using non-Rayleigh scattering at 95 GHz. *J. Atmos. Oceanic Technol.*, 27,
942 1490–1503.

943 Giangrande, S. E., E. P. Luke, and P. Kollias, 2012: Characterization of Vertical Velocity and
944 Drop Size Distribution Parameters in Widespread Precipitation at ARM Facilities. *J. Appl.*
945 *Meteor. Climatol.*, 51, 380–391, <https://doi.org/10.1175/JAMC-D-10-05000.1>.

946 Giangrande, S. E., S. Collis, J. Straka, A. Protat, C. Williams, and S. Krueger (2013), A summary
947 of convective-core vertical velocity properties using ARM UHF wind profilers in
948 Oklahoma, *J. Appl. Meteorol. Climatol.*, 52, 2278–2295.

949 Giangrande, S. E., Toto, T., Jensen, M. P., Bartholomew, M. J., Feng, Z., Protat, A., Williams, C.
950 R., Schumacher, C., and Machado, L. (2016), Convective cloud vertical velocity and mass-
951 flux characteristics from radar wind profiler observations during GoAmazon2014/5, *J.*
952 *Geophys. Res. Atmos.*, 121, 12,891–12,913, doi:10.1002/2016JD025303.

953 Giangrande, S. E., Wang, D., Bartholomew, M. J., Jensen, M. P., Mechem, D. B., Hardin, J. C., &
954 Wood, R. (2019). Midlatitude oceanic cloud and precipitation properties as sampled by the
955 ARM Eastern North Atlantic Observatory. *Journal of Geophysical Research: Atmospheres*,
956 124, 4741–4760. <https://doi.org/10.1029/2018JD029667>

957 Goddard, J. W. F., Tan J., and Thurai M. , 1994: Technique for calibration of meteorological radar
958 using differential phase. *Electron. Lett.*, 30 , 166–167.

959 Gorgucci, E., R. Bechini, L. Baldini, R. Cremonini, and V. Chandrasekar, 2013: The Influence of
960 Antenna Radome on Weather Radar Calibration and Its Real-Time Assessment. *J. Atmos.*
961 *Oceanic Technol.*, 30, 676–689, <https://doi.org/10.1175/JTECH-D-12-00071.1>.

962 Dupont, J.C. M. A. Drouin, J.F. Ribaud, A. Gibe, J. Delanoe, F. Toledo, L. Pfitzenmaier, G.
963 Ghiggi, M. Schleiss: 2022 Hands-on training » on the monitoring of stability of DCR
964 reflectivity using disdrometers ACTRIS-CCRES workshop, November 14-15th 2022,
965 SIRTA Observatory.

966

967 Hardin, J., A. Hunzinger, E. Schuman, A. Matthews, N. Bharadwaj, A. Varble, K. Johnson, and
968 S. Giangrande, 2020: CACTI Radar b1 Processing: Corrections, Calibrations, and
969 Processing Report. Tech. Doc. DOE/SC-ARM-
970 TR244, 46 pp., <https://arm.gov/publications/brochures/doe-sc-arm-tr-244.pdf>.

971 Hardin, J., Giangrande, S. E., and Zhou, A. Laser Disdrometer Quantities (LDQUANTS) and
972 Video Disdrometer Quantities (VDISQUANTS) Value-Added Products Report. United
973 States: N. p., 2020. Web. doi:10.2172/1808573.

974 Hunzinger, A, JC Hardin, N Bharadwaj, A Varble, and A Matthews. 2020. “An Extended Radar
975 Relative Calibration Adjustment (eRCA) Technique for Higher Frequency Radars and RHI
976 Scans.” *Atmospheric Measurement Techniques Discussions*, [https://doi.org/10.5194/amt-](https://doi.org/10.5194/amt-2020-57)
977 2020-57

978 Jensen, M. P., D. Collins, P. Kollias, D. Rosenfeld, A. Varble, S. Collis, J. Fan, R. Griffin, R.
979 Jackson, T. Logan, G. McFarquhar, J. Quaas, R. Sheesley, P. Stier, S. van den Heever, Y.

980 Wang, G. Zhang, E. Bruning, A. Fridlind, C. Kuang, A. Ryzkhov, S. Brooks, . Defer, S.
981 E. Giangrande, J. Hu, M. Kumjian, T. Matsui, C. Nowotarski, M. Oue,, J. Snyder, S.
982 Usenko, M. van Lier Walqui, and Y. Xu, 2019: TRacking Aerosol Convection Interactions
983 Experiment (TRACER) Science Plan. DOE/SC-ARM-19-017. 30 pp.

984 Jensen, M. P., L. Judd, P. Kollias, J. Sullivan, R. Nadkarni, C. Kuang, G. McFarquhar, H. Powers
985 and J. Flynn, 2022: A succession of cloud, precipitation, aerosol and air quality field
986 experiments in the coastal urban environment. Bull. Amer. Meteor. Soc.,
987 <https://doi.org/10.1175/BAMS-D-21-0104.1>.

988 Jensen, M. P., J. H. Flynn, P. Kollias, C. Kuang, G. McFarquhar, H. Powers, S. Brooks, E. Bruning,
989 D. Collins, S. M. Collis, J. Fan, A. Fridlind, S. E. Giangrande, R. Griffin, J. Hu, R. C.
990 Jackson, M. Kumjian, T. Logan, T. Matsui, C. Nowotarski, M. Oue, A. Rapp, D. Rosenfeld,
991 A. Ryzhkov, R. Sheesley, J. Snyder, P. Stier, S. Usenko, S. van den Heever, M. van Lier-
992 Walqui, A. Varble, Y. Wang, A. Aiken, M. Deng, D. Dexheimer, M. Dubey, Y. Feng, V.
993 Ghate, K. L. Johnson, K. Lamer, S. Saleeby, D. Wang, M. Zawadowicz and A. Zhou, 2023:
994 TRacking Aerosol Convection interactions ExpeRiment (TRACER) final campaign report.
995 DOE/SC-ARM-3-038. 132 pp.

996
997 Kollias, P., Bharadwaj N., Widener K. , Jo I. , and Johnson K. , 2014a: Scanning ARM cloud
998 radars. Part I: Operational sampling strategies. J. Atmos. Oceanic Technology, in press.

999 Kollias, P., and Coauthors, 2014b: Scanning ARM Cloud Radars. Part II: Data Quality Control
1000 and Processing. J. Atmos. Oceanic Technol., 31, 583–
1001 598, <https://doi.org/10.1175/JTECH-D-13-00045.1>.

1002 Kollias, P., E. E. Clothiaux, M. A. Miller, B. A. Albrecht, G. L. Stephens, and T. P. Ackerman,
1003 2007: Millimeter-Wavelength Radars: New Frontier in Atmospheric Cloud and
1004 Precipitation Research. Bull. Amer. Meteor. Soc., 88, 1608–
1005 1624, <https://doi.org/10.1175/BAMS-88-10-1608>.

1006 Kollias, P., and Coauthors, 2020: The ARM Radar Network: At the Leading Edge of Cloud and
1007 Precipitation Observations. Bull. Amer. Meteor. Soc., 101, E588–
1008 E607, <https://doi.org/10.1175/BAMS-D-18-0288.1>.

- 1009 Kollias, P., B. P. Treserras, and A. Protat, 2019: Calibration of the 2007–2017 record of
1010 Atmospheric Radiation Measurements cloud radar observations using CloudSat,
1011 Atmospheric Measurement Techniques, 12, 4949–4964, <https://doi.org/10.5194/amt-12-4949-2019>
- 1013 Kurri, M., and A. Huuskonen, 2008: Measurements of the transmission loss of a radome at
1014 different rain intensities. *J. Atmos. Oceanic Technol.*, 25, 1590–1599.
- 1015 Lamer, K., Mariko Oue, Alessandro Battaglia, Richard J. Roy, Ken B. Cooper, Ranvir
1016 Dhillon, and Pavlos Kollias 2021: Multifrequency radar observations of clouds and
1017 precipitation including the G-band. *Atmospheric Measurement Techniques*. Volume 14,
1018 issue 5 AMT, 14, 3615–3629, 2021 <https://doi.org/10.5194/amt-14-3615-2021>
- 1019 Lhermitte, R., 2002: Centimeter and Millimeter Wavelength Radars in Meteorology. Lhermitte
1020 Publications, 550 pp.
- 1021 Liu, Y. and Mace, G. G.: Assessing synergistic radar and radiometer capability in retrieving ice
1022 cloud microphysics based on hybrid Bayesian algorithms, *Atmos. Meas. Tech.*, 15, 927–
1023 944, <https://doi.org/10.5194/amt-15-927-2022>, 2022.
- 1024 Louf, V., A. Protat, R. A. Warren, S. M. Collis, D. B. Wolff, S. Raunyar, C. Jakob, and W. A.
1025 Petersen, 2019: An Integrated Approach to Weather Radar Calibration and Monitoring
1026 Using Ground Clutter and Satellite Comparisons. *J. Atmos. Oceanic Technol.*, 36, 17–
1027 39, <https://doi.org/10.1175/JTECH-D-18-0007.1>.
- 1028 Luca Baldini, V. Chandrasekar & Dmitri Moisseev (2012) Microwave radar signatures of
1029 precipitation from S band to Ka band: application to GPM mission, *European Journal of*
1030 *Remote Sensing*, 45:1, 75-88, DOI: 10.5721/EuJRS20124508
- 1031 Maahn, M., Hoffmann, F., Shupe, M. D., de Boer, G., Matrosov, S. Y., and Luke, E. P.: Can liquid
1032 cloud microphysical processes be used for vertically pointing cloud radar calibration?,
1033 *Atmos. Meas. Tech.*, 12, 3151–3171, <https://doi.org/10.5194/amt-12-3151-2019>, 2019.

1034 Matrosov, S. Y., 2005: Attenuation-Based Estimates of Rainfall Rates Aloft with Vertically
1035 Pointing Ka-Band Radars. *J. Atmos. Oceanic Technol.*, 22, 43–
1036 54, <https://doi.org/10.1175/JTECH-1677.1>.

1037 Matthews, A., M. Deng, E. Schuman, Y.Feng, M. Rocque, 2024: SAIL Radar B1 Processing:
1038 Corrections, Calibrations, and Processing Report. U.S. Department of Energy,
1039 Atmospheric Radiation Measurement user facility, Richland, Washington. In preparation.

1040 Mead, J. 2010. MMCR Calibration Study. U.S. Department of Energy. DOE/SC-ARM/TR-088.

1041 Meagher, Jonathan P., and Ziad S. Haddad. “To What Extent Can Raindrop Size Be Determined
1042 by a Multiple-Frequency Radar?” *Journal of Applied Meteorology and Climatology*, vol.
1043 45, no. 4, 2006, pp. 529–36. JSTOR, <http://www.jstor.org/stable/26171702>. Accessed 13
1044 Mar. 2023.

1045 Miller, M. A., K. Nitschke, T. P. Ackerman, W. R. Ferrell, N. Hickmon, and M. Ivey, 2016: The
1046 ARM Mobile Facilities. *Meteor. Monogr.*, 57, 9.1–
1047 9.15, <https://doi.org/10.1175/AMSMONOGRAPHS-D-15-0051.1>.

1048 Muradyan, P., and Coulter, R.: Radar Wind Profiler (RWP) and Radio Acoustic Sounding System
1049 (RASS) instrument handbook, U. S. Department of Energy, Atmospheric Radiation
1050 Measurement user facility, DOE/SC-ARM-TR-044, <https://doi.org/10.2172/1020560>,
1051 2020.

1052 Myagkov, A., Kneifel, S., and Rose, T.: Evaluation of the reflectivity calibration of W-band radars
1053 based on observations in rain, *Atmos. Tech.*, 13, 5799–5825, [https://doi.org/10.5194/amt-](https://doi.org/10.5194/amt-13-5799-2020)
1054 [13-5799-2020](https://doi.org/10.5194/amt-13-5799-2020), 2020.

1055 Protat, A., D. Bouniol, E. J. O’Connor, H. Klein Baltink, J. Verlinde, and K. Widener, 2011:
1056 CloudSat as a Global Radar Calibrator. *J. Atmos. Oceanic Technol.*, 28, 445–452,
1057 <https://doi.org/10.1175/2010JTECHA1443.1>.

1058 Rocque, M. M. Deng, Y.Feng, E. Schuman, I. Silber, A. Matthews, T. Wendler, V. Castro, Iosif
1059 Lindenmaier, 2024: ECAPE Radar b1 Processing: Corrections, Calibrations, and

1060 Processing Report, U.S. Department of Energy, Atmospheric Radiation Measurement user
1061 facility, Richland, Washington. In preparation.

1062 Ryzhkov, AV, SE Giangrande, VM Melnikov, and TJ Schuur. 2005. "Calibration Issues of Dual-
1063 Polarization Radar Measurements." *Journal of Atmospheric and Oceanic Technology*
1064 22(8): 1138– 1155, <https://doi.org/10.1175/JTECH1772.1>

1065 Segelstein, D. J., "The complex refractive index of water," University of Missouri-Kansas City,
1066 (1981).

1067 Thompson, R., A. Illingworth, T. Darlington, and J. Ovens, 2012: Correcting attenuation in
1068 operational radars from both heavy rain and the radome using the observed microwave
1069 emission. *Proc. Seventh European Conf. on Radar in Meteorology and Hydrology*,
1070 Toulouse, France, ERAD, 8A.5.

1071 Tridon, F., Battaglia, A., Kollias, P., Luke, E., and Williams, C. R.: Signal postprocessing and
1072 reflectivity calibration of the Atmospheric Radiation Measurement Program 915-MHz
1073 Wind Profilers, *J. Atmos. Ocean. Tech.*, 30, 1038-1054. <https://doi.org/10.1175/JTECH->
1074 [D-12-00146.1](https://doi.org/10.1175/JTECH-D-12-00146.1), 2013.

1075 Ulaby, F. T., R.K. Moore, and A.K. Fung, 1981: *Microwave Remote Sensing*. Vol. 1, Addison-
1076 Wesley, 456pp.

1077 Varble, A. C., and Coauthors, 2021: Utilizing a Storm-Generating Hotspot to Study Convective
1078 Cloud Transitions: The CACTI Experiment. *Bull. Amer. Meteor. Soc.*, 102, E1597–
1079 E1620, <https://doi.org/10.1175/BAMS-D-20-0030.1>.

1080 Wang D, S Giangrande, M Bartholomew, J Hardin, Z Feng, R Thalman, and L Machado.
1081 2018. "The Green Ocean: precipitation insights from the GoAmazon2014/5
1082 experiment." *Atmospheric Chemistry and Physics*, 18(12), 10.5194/acp-18-9121-2018.

1083 Wang D, S Giangrande, Bartholomew, J Hardin 2021: Analysis of Three Types of Collocated
1084 Disdrometer Measurements at the ARM Southern Great Plains Observatory, DOE/SC-
1085 ARM-TR-275. <https://www.arm.gov/publications/programdocs/doe-sc-arm-tr-275.pdf>

1086 Widener, K. B. and J. B Mead 2004: W-Band ARM Cloud Radar – Specifications and Design
1087 Fourteenth ARM Science Team Meeting Proceedings, Albuquerque, New Mexico, March 22-26,
1088 Widener, K., N Bharadwaj, and K. Johnson, 2012: Ka-Band ARM Zenith Radar (KAZR)
1089 handbook. DOE/SC-ARM/TR-106
1090 https://www.arm.gov/publications/tech_reports/handbooks/kazr_handbook.pdf

1091 Wolff, DB, DA Marks, and WA Petersen. 2015. “General Application of the Relative Calibration
1092 Adjustment (RCA) Technique for Monitoring and Correcting Radar Reflectivity
1093 Calibration.” *Journal of Atmospheric and Oceanic Technology* 32(3): 496–506,
1094 <https://doi.org/10.1175/JTECH-D-13-00185.1>

1095 Williams, C. R., Gage, K. S., Clark, W., and Kucera, P.: Monitoring the reflectivity calibration of
1096 a scanning radar using a profiling radar and a disdrometer, *J. Atmos. Oceanic Technol.*, 22,
1097 1004-1018, 2005.

1098 Williams, C.R., Barrio, J., Johnston, J. E., Myradyan, P. and Giangrande, S. E.: Calibrating radar
1099 wind profiler reflectivity factor using surface disdrometer observations, *J. Atmos. Meas.*
1100 *Techn.*, in review, <https://egusphere.copernicus.org/preprints/2023/egusphere-2022-1405>,
1101 2023.

1102 Xingjian Yu, Yu Zhang, Run Hu, Xiaobing Luo, 2021: Water droplet bouncing dynamics, *Nano*
1103 *Energy*, Volume 81, 2021, 105647, ISSN 2211-
1104 2855, <https://doi.org/10.1016/j.nanoen.2020.105647>.

1105 Zhang, G., J. Vivekanandan and E. Brandes, "A method for estimating rain rate and drop size
1106 distribution from polarimetric radar measurements," in *IEEE Transactions on Geoscience*
1107 *and Remote Sensing*, vol. 39, no. 4, pp. 830-841, April 2001, doi: 10.1109/36.917906.

1108 Zhu, Z., Lamer, K., Kollias, P., & Clothiaux, E. E. (2019). The vertical structure of liquid water
1109 content in shallow clouds as retrieved from dual-wavelength radar observations. *Journal of*
1110 *Geophysical Research:*
1111 *Atmospheres*, 2019; 124: 14184– 14197. <https://doi.org/10.1029/2019JD031188>

